Phase behaviour, thermal expansion and compressibility of $SnMo_2O_8$

Luiza R. Araujo[a], Leighanne C. Gallington[b,c], Angus P. Wilkinson[b,d], John S. O. Evans*[a]

a Department of Chemistry, Durham University, Science Laboratories, South Road, Durham DH1 3LE, United Kingdom

b School of Chemistry and Biochemistry, Georgia Institute of Technology, Atlanta, GA 30332-0400, United States

c Current address: X-ray Science Division, Advanced Photon Source, Argonne National Laboratory, Argonne, IL 60439-4858, United States.

d School of Materials Science and Engineering, Georgia Institute of Technology, Atlanta, GA 30332-0245, United States

0. Abstract

The phase behaviour and thermoelastic properties of $SnMo_2O_8$, derived from variable temperature and pressure synchrotron powder diffraction data, are reported. $SnMo_2O_8$ is a member of the AM_2O_8 family of negative thermal expansion (NTE) materials, but unexpectedly, has positive thermal expansion. Over the *P-T* space explored (298–513 K, ambient to 310 MPa) four different forms of $SnMo_2O_8$ are observed: *α*, *β*, *γ* and *γ*'. The *γ* to *β* transition is temperature-, pressure-, and time-dependent. $SnMo_2O_8$ is a much softer material (*α* and *γ* form have B_T = ~29 and 26 GPa at 298 K) than other members of the AM_2O_8 family. Counter-intuitively, its high temperature *β* phase becomes stiffer with increasing temperature (B_T = ~36 GPa at 490 K). The pressure dependence of the thermal expansion for each phase is reported.

Keywords: Zero thermal expansion, Negative Thermal Expansion, Thermoelastic properties, Phase transitions, Tin molybdate.

Highlights: $SnMo_2O_8$ is of interest as an end member of the $Zr_{1-x}Sn_xMo_2O_8$ zero thermal expansion family of materials. $SnMo_2O_8$ is significantly softer than other members of the AM_2O_8 family with a bulk modulus at 298 K of ~29 GPa. The bulk modulus increases as temperature is increased such that $SnMo_2O_8$ shows the unusual behaviour of "warm-hardening". This behaviour is explained in terms of the pressure and temperature driven order-disorder phase transitions it undergoes.

1. Introduction

This paper reports an in-situ X-ray diffraction study probing the phase stability and properties of $SnMo_2O_8$ polymorphs. $SnMo_2O_8$ is the end member of a solid solution ($Zr_{1-x}Sn_xMo_2O_8$) which can be systematically tuned to show either positive, negative or essentially zero

thermal expansion over a broad temperature range of ~2–800 K [1]. In order for ceramic bodies based on $SnMo_2O_8$ to find application, the behaviour of the material as a function of temperature, pressure and time must be understood. The phase regions of $SnMo_2O_8$ have therefore been mapped out at temperatures from 298 to 513 K and pressures from ambient up to 310 MPa, and the conditions under which the α, γ, γ' and β phases are kinetically stable have been determined. The bulk modulus of each phase and the pressure-dependence of their thermal expansion is reported. We find that β-$SnMo_2O_8$ shows the unusual property of "warm hardening" whereby its bulk modulus or stiffness increases with temperature – this is the opposite behaviour to most known materials [2-5].

The cubic AM_2O_8 family of materials (A = Zr, Hf; M = Mo, W) is well known for displaying strong, reversible and isotropic negative thermal expansion (NTE) [6-9]. ZrW_2O_8, for example, contracts from 2 to 1070 K with a linear expansion coefficient of $\alpha_l = -9\times10^{-6}$ K^{-1} (0–350 K) [10]. To understand the various contributions to the thermal contraction of this family, it is worth considering the thermodynamic relationship between the volumetric thermal expansion coefficient, α_V, and the bulk modulus B ($B_T = 1/\text{compressibility} = -V(\partial P/\partial V)_T$):

$$\alpha_V = \frac{1}{V}\left(\frac{\partial V}{\partial T}\right)_P = \frac{1}{B_T}\left(\frac{\partial S}{\partial V}\right)_T \qquad [1]$$

For a stable material B_T is a positive quantity, which implies a direct relationship between the sign of α_V and whether entropy increases or decreases with volume. If we consider the role of phonons, their effect on thermal expansion is usually described via the Grüneisen parameter $\gamma_i = -\partial \ln\omega_i / d\ln V$ which captures how the frequency of a mode (ω_i) depends on volume (V), and can be related to thermal expansion via the relationship $\alpha_V = C_V\overline{\gamma}/BV$, where $\overline{\gamma}$ is the mean Grüneisen parameter of the material (typically around 1) and C_V its heat capacity at constant volume [2, 11]. The relationship to entropy arises as mean squared atomic displacements are proportional to $1/\omega^2$ such that for a negative-Grüneisen-parameter mode, decreasing volume will lead to decreasing ω, larger atomic displacements and increased entropy. In fact, $\overline{\gamma}$ can be related to entropy via the expression $\overline{\gamma} = \frac{V}{C_V}\left(\frac{\partial S}{\partial V}\right)_T$, which emphasizes the link between the signs of $\overline{\gamma}$, $\left(\frac{\partial S}{\partial V}\right)_T$ and (via equation 1) α_V.

In the simplest local picture of AM_2O_8 materials, the negative Grüneisen parameter modes can be linked to transverse vibrations of A–O–M bridging oxygens. In a more extended view, we can consider these vibrations occurring via the correlated motions of rigid or quasi-rigid polyhedra, so called rigid unit modes RUMs or qRUMs respectively [2, 12-14]. A full

understating of (N)TE can, however, only be achieved by considering phonon modes throughout the entire Brillouin zone, and recent publications have presented methods for visualising the contributions of different modes to NTE and the degree to which framework polyhedra are distorted in materials such as AM_2O_8 and $A_2(MO_4)_3$ [2, 15, 16]. The general relationship between α_V and $(\partial S/\partial V)_T$ also highlights the fact that other considerations such as spin disorder in magnetic materials or, for the AM_2O_8 family, polyhedral orientational disorder, will influence thermal expansion. A final intriguing aspect of NTE materials is that one might find either the counter-intuitive effect of pressure-induced softening [$B_0^{'} = (\partial B/\partial P)_{P=0}$ negative] [17-21] or anharmonicity leading to increasing bulk modulus with temperature [$(\partial B/\partial T)$ >0] a phenomenon which has been termed "warm hardening" [2]. To date only a small number of examples of warm hardening have been reported, see for example $Sc_{1-x}Al_xF_3$ [3], β-HfW_2O_8 [4] and ZrV_2O_7 [5].

There are several reasons why pressure is an important experimental variable in understanding negative thermal expansion materials. Firstly, as discussed above, high pressure experiments can be used to probe the phonons responsible for NTE through direct measurement of the volume dependence of their frequency in order to determine the sign of the mode Grüneisen parameter; there have been many such studies on NTE materials [22-25]. Secondly, the relatively open frameworks of NTE materials, along with the requirement for low frequency modes that soften on volume reduction, often leads to pressure-induced phase transitions to new crystalline or amorphous phases at low pressures. These will typically have different thermal expansion properties and could potentially alter the properties of pure ceramics or composites. In the AM_2O_8 family, ZrW_2O_8 has been shown to undergo irreversible (at room temperature) transitions to either a *γ* phase with a ~5% volume reduction at ~0.2 GPa [26], an amorphous form [27] or (at elevated *T*) to a dense U_3O_8-structured phase [28]. For $ZrMo_2O_8$ and $HfMo_2O_8$ various phase transitions have been observed under pressure [29-33]. Finally, many of the thermally-driven phase transitions in AM_2O_8 materials are of an order-disorder type and as such are strongly influenced by pressure due to the associated volume change, $\Delta V_{\text{disorder}}$. The influence of pressure on phase stability can be captured via the thermodynamic relationship $\mathrm{dG} = \mathrm{Vd}P - \mathrm{Sd}T$ leading to $\left(\partial \Delta G_{\text{disorder}}/\partial P\right)_T = \Delta V_{\text{disorder}}$ [34].

A cubic form of $SnMo_2O_8$ was first reported in 1988 [35], but its structure and thermal expansion properties were only recently examined [1]. The normal room and high temperature forms of $SnMo_2O_8$ (*α* and *β* respectively) are closely related to high temperature cubic *β*-ZrW_2O_8 [6] and cubic *γ*-$ZrMo_2O_8$ [8], Figure 1, but $SnMo_2O_8$ is unique among cubic

AM_2O_8 phases in showing positive thermal expansion at all temperatures. This property is exploitable in that solid solutions $Zr_{1-x}Sn_xMo_2O_8$ can be systematically tuned from negative to zero (around x = 0.5) and then to positive thermal expansion (Figure 1c).

In addition to the cubic forms, careful in-situ diffraction studies have shown that the ambient pressure (non-equilibrium) phase diagram of $SnMo_2O_8$ is remarkably complex, with structure showing a strong dependence on thermal history. The behaviour is summarised in Figure 1d. On heating, a "normal" room temperature cubic sample - the *α* phase - shows positive expansion and undergoes a phase transition to a high temperature *β* phase (isostructural with *β*-ZrW_2O_8 and, by analogy, likely to be dynamically disordered [36]) at around 330 K. If the sample is cooled at "normal" rates (minutes to hours to cool from 400 K to room temperature) this transition is reversible. Quenching the sample from T > 400 K produces a metastable cubic form – the *α*' phase – whose cell parameter and therefore structure evolves very slowly (weeks to years at room temperature) towards the *α* phase. If *α or α*'-$SnMo_2O_8$ are held for extended periods in a small temperature window around 390 K, there is a slow phase transition to a rhombohedral structure, the *γ* phase. *γ*-$SnMo_2O_8$ has the same connectivity of corner-sharing AO_6 octahedra and tetrahedra as the cubic materials (Figure 1b) but contains a specific ordering pattern of pairs of MO_4 tetrahedra (O_3M–O···O_3M–O) relative to the <111> axes of the high temperature disordered structure. This causes a reduction in symmetry to $R\bar{3}$ and the *γ* structure can be described in terms of a cell with $a = b = c \approx \sqrt{2}a_{\text{cubic}}; \alpha = \beta = \gamma \approx 59.3°$ or an equivalent R-centred hexagonal cell with $a = b = \sqrt{2}a_{\text{cubic}}, c = 2\sqrt{3}a_{\text{cubic}}; \alpha = \beta = 90, \gamma \approx 120°$. Once formed, the lower-volume *γ* phase is stable indefinitely at room temperature but, reverts to the cubic *β* phase on heating to ~440 K. The room temperature *α* phase is best viewed as a trapped or glassy structure that may evolve to an ordered *γ* phase over infinite time.

In this paper, we report the pressure dependence of the phase stability regions of $SnMo_2O_8$ samples prepared by two different synthetic routes. One route follows that described by Buiten [35] in which $SnCl_{4(g)}$ is reacted with $MoO_{3(s)}$ in a flowing oxygen stream - the gas-solid route; the second is *via* heat treatment of an amorphous precursor, as described by Tallentire *et al* [1]. Variable (P,T) X-ray diffraction studies are reported for samples prepared initially in the cubic *α* phase by both methods and on a sample prepared by the gas-solid route then converted to the rhombohedral *γ* phase.

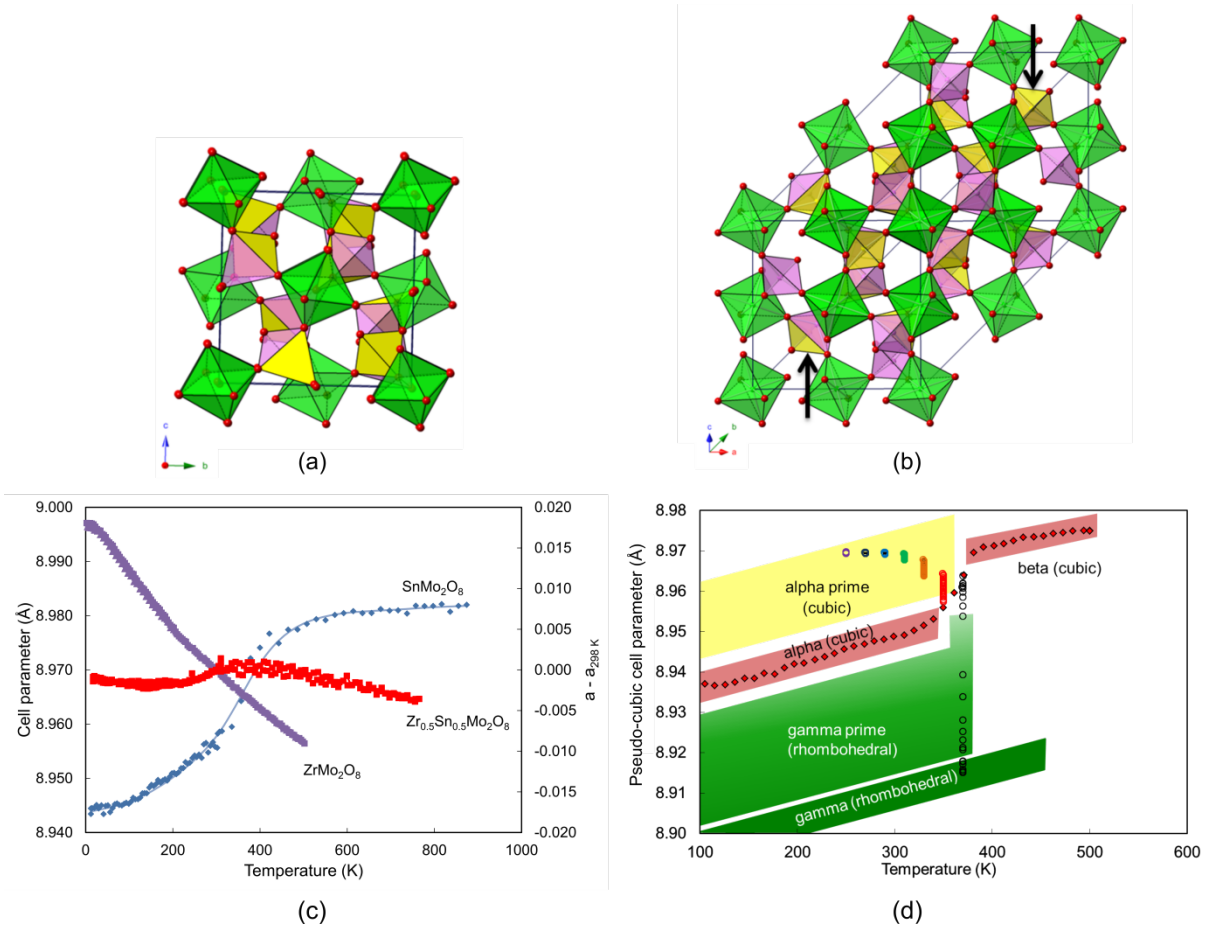

Figure 1. (a, b) Cubic (*α/β*) and rhombohedral (*γ*) structures of $SnMo_2O_8$. Octahedral groups (SnO_6) are shown in green and tetrahedral groups (MoO_4) in yellow/pink; small red spheres represent oxygen atoms. In the cubic phase, the tetrahedral groups are statically (*α*) or presumed dynamically (*β*) disordered between the yellow and pink orientation. In the rhombohedral phase, the tetrahedral groups are ordered along the <111> axes of the original cubic cell occupying the yellow sites in (b). Note that the upper arrowed occupied site points in opposite direction relative to the cubic structure. (c) The thermal expansion of $SnMo_2O_8$ (left-hand axis) at ambient pressure in comparison with the x = 0.5 member of the $Zr_{1-x}Sn_xMo_2O_8$ solution and $ZrMo_2O_8$ (right-hand axis). (d) Phase-stability regions of $SnMo_2O_8$ at ambient pressure as derived from unit cell parameters. Normal low and high temperature forms are cubic *α* and β phases. A small temperature window exists in which it is possible to convert to a rhombohedral *γ* phase. The *α*' phase can be formed by quenching from high temperature. *α, α*' and *γ*' phases evolve slowly over time.

2. Experimental section

2.1 Samples investigated

$SnMo_2O_8$ was prepared via two different synthetic methods which we call the gas-solid route and the precursor route. Both methods have been previously described [1, 35]. In the solid-state route, a typical reaction involved placing $MoO_{3(s)}$ (Alfa Aesar, 99.95%, 1.500 g) in a crucible inside an amorphous silica tube in a tube furnace at 773 K. Sulfuric acid was used

to dry O_2 which was used as a carrier gas to flow $SnCl_{4(g)}$ (Acros Organics, 99% Anhydrous) over MoO_3 for a period of 7 h.

For the precursor route, a typical synthesis involved separately dissolving stoichiometric amounts of $(NH_4)_6Mo_7O_{24}.4H_2O_{(s)}$ (Alfa Aesar, 99.999%) and $SnCl_4.5H_2O_{(s)}$ (Sigma Aldrich, 98%) in 12 ml of distilled water. The two solutions were then added to 6 ml of distilled water, which was cooled to ~5 °C, with continuous stirring for ~20 min. The resulting white precipitate was then filtered and dried at 373 K overnight. Crystalline $SnMo_2O_8$ was obtained by heating this amorphous precursor to 863 K for 30 min. Phase purity and identity was confirmed by X-ray diffraction of the crystalline materials. Powder diffraction experiments with a crystalline internal standard show the amorphous content of these samples to be <5 %. A sample of *α* phase material, which had been prepared by the gas-solid route, was converted to the *γ* phase by heating at 390 K for 32 h.

2.2 Experimental setup and data collection

Variable temperature and pressure powder X-ray diffraction data were collected at beamline 11-ID-B (58.65 keV, 0.2114 Å x-rays) of the Advanced Photon Source (APS), Argonne National Laboratory. The samples were mixed with silicone oil and loaded into Kapton capillaries. The sample environment used to access the pressures and temperatures has been previously described [37].

The phase behaviour of samples synthesised using both methods were explored between 298 and 513 K at pressures from 52 to 310 MPa. Each sample was heated to a set temperature and datasets recorded on compression at 103, 207 and 310 MPa then decompression at 259, 155, 52 MPa. The different *T* intervals investigated in each experiment are specified in Figure 5a-d. For the gas-solid route, the phase behaviour of samples initially in the *α* phase (experiment 1) and *γ* phase (experiment 2) were investigated, whilst for the precursor route sample, the phase behaviour of the *α* phase (experiments 4 and 5) and the kinetics of the *β*→*γ* transition were explored (at 422 K and 310 MPa for 6.5 h, experiment 3).

2.3 Rietveld refinement

To allow systematic Rietveld analyses of all the data, a single model was used to fit datasets containing either the cubic or rhombohedral phases. A rhombohedral description of the *γ* structure in space group $R\bar{3}$ was used with cell parameters of *a* ~12.60 Å and *α* ~60.0°. To allow either cubic or rhombohedral phases to be described, *α* was allowed to refine between 59.3 and 60.0°.

To describe the different ordering of the Mo_2O_8 groups in the cubic and gamma structures, a fractional site occupancy was refined for the tetrahedral pairs. We discuss the sensitivity of this parameter to the experimental data in section 3.1. To account for the peak broadening arising from compression and decompression, a single Lorentzian strain parameter was convoluted with an empirical pseudo-Voigt instrumental profile peak shape determined using a CaF_2 standard. A small region ($2\theta \approx 9.45$ to $9.65°$) containing parasitic scattering from the pressure vessel was excluded from the analyses. 12 terms of a Chebyshev polynomial were used to model the background, one scale factor and one isotropic atomic displacement for all atoms were refined. For the structural model, one lattice parameter and one cell angle were refined in addition to 56 atomic coordinates. To make sure polyhedral connectivity was maintained without major distortions, polyhedral restraints were applied on bond distances and angles of the SnO_6 octahedra and MoO_4 tetrahedra. With the relatively low resolution of this experimental set up it is possible to extract high quality information on the phases present under any conditions, but detailed structural information is not available. Atomic coordinates used in the fits are given in the supplementary information together with tables of refined cell parameters under the different experimental conditions (Tables S1-S5). All Rietveld analyses were performed with the Topas Academic software [38, 39]. This model gave a stable refinement and excellent fit for most datasets. There were no significant changes in Rietveld scale factors to indicate significant amorphisation. A small number of datasets close to phase boundaries showed the presence of two phases. These were analysed with a two phase model and are discussed in section 3.2.

3. Results and discussion

3.1 Rietveld refinement and Mo_2O_8 ordering evolution: overall observations

Figure 2a shows a typical pseudo film plot of XRD patterns obtained in experiment 1 displayed in the order that they were measured; temperature therefore increases then decreases from bottom to top and pressure rises then falls at each *T*. The zig-zag of the peak positions is related to the compression and decompression steps, where the peaks either shift to the right when the material is being compressed, or to the left, when it is being decompressed. In the initial low *P*, *T* regions of our experiments, sharp single diffraction peaks are observed consistent with a cubic material. It is clear from the plot that a phase transition to the gamma structure occurs in intermediate regions of *P*, *T* space as seen from the splitting of 2θ ~7.6, 10.2 or 10.4° peaks, followed by reversion to a cubic structure at the highest temperatures. Figure 2b shows typical Rietveld refinements obtained for the *α*, *γ* and an intermediate *γ'* phase, which are discussed in section 3.1.1.

Figure 3 summarises the results from Rietveld analysis of the 96 datasets shown in

Figure 2, along with a further 375 datasets from other experiments (shown in SI, Fig. S1). Figure 3a shows two key structural parameters as a function of temperature: the ordering of Mo_2O_8 groups and the rhombohedral cell angle *α*. In this plot, Mo_2O_8 ordering is expressed as 2×(fractional occupancy – 0.5) and can be thought of as an order parameter expressing the degree of cubic (0.0) or gamma (1.0) ordering. Mo_2O_8 ordering shows a smooth evolution from the disordered cubic *α* phase at low *T* to ordered *γ* at intermediate *T* before reverting to cubic *β* at high *T* (Figure 1d). There is a strong correlation between the refined cell angle *α* (60.0° in cubic phases; 59.3° in *γ*) and the degree of orientational ordering. The strong correlation between cell angle and Mo_2O_8 ordering is further shown in Figure 3b which plots cell angle against Mo_2O_8 fractional occupancy for all 375 datasets recorded. The smooth trend in points on this plot gives us confidence that the structural model used in the Rietveld analyses allows the phase behaviour of $SnMo_2O_8$ to be mapped out for all experiments.

As there is a smooth evolution from cubic disordered Mo_2O_8 phases towards fully ordered *γ*-$SnMo_2O_8$ (at least at the resolution and on the timescale of these experiments) we describe samples intermediate between cubic and rhombohedral as *γ'* for convenience.

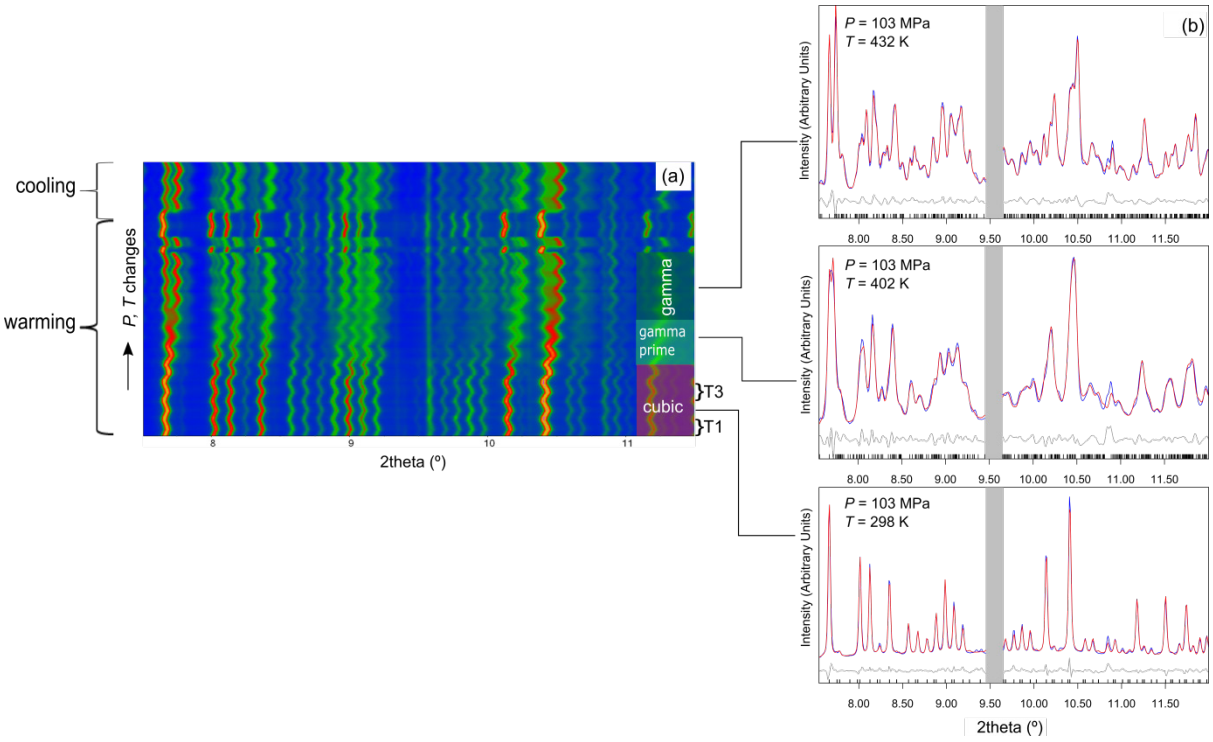

Figure 2. (a) Pseudo film plot of X-ray patterns with intensity represented by a color scale, under compression (peaks shift to the right) and decompression (peaks shift to the left) in experiment 1. Data were collected on warming (first 72 of 96 sets) and cooling (last 24 sets). Examples of isothermal segments during which pressure was varied are shown with curly brackets on the right of the plot and labelled as T1 or T3. Conditions where the cubic/rhombohedral phases are present can be clearly seen from, for example, the presence

of single or split peaks at 2θ ~7.6, 10.2 or 10.4°. (b) Rietveld fits to selected datasets showing the *α*, *γ'* and *γ* structures, from bottom to top, respectively. Observed data is shown in blue, calculated in red, difference in gray and tick marks indicating reflection positions in black. The gray bars indicate the excluded region containing parasitic scattering from the pressure vessel.

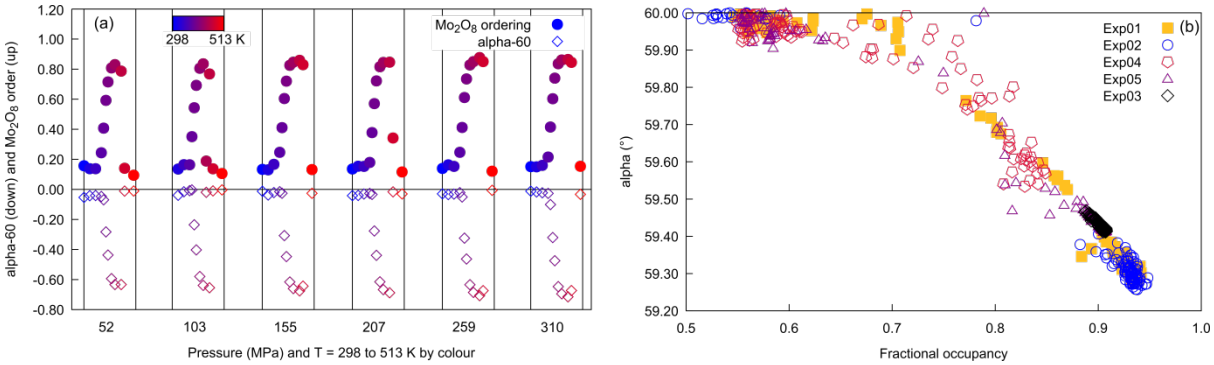

Figure 3. (a) Dependence of Mo_2O_8 group ordering on pressure and temperature in experiment 1 for data collected on warming. The gradual reduction in cell angle, *α*, as Mo_2O_8 groups start to order at intermediate temperatures can be seen, highlighting the correlations summarised in (b). (b) Scatter plot of cell angle *α* and fractional occupancy using data points on heating and cooling for experiment 1 (orange squares) alongside the values obtained from all other experiments, showing the strong correlation between the two parameters. The Mo_2O_8 ordering in the *γ* phase is defined as 2*(frac-0.5), where frac is the single fractional occupancy parameter refined. Given the data quality, a refined fractional occupancy of ~0.94 represents essentially full order.

3.1.1 Intermediate phase: the partial ordering of the gamma structure

Early experiments suggested that the *β*→*γ* phase transition was kinetically sluggish under some conditions. This was investigated by holding the temperature and pressure of a *β* phase sample at 422 K and 310 MPa for ~6.5 h. Figure 4a shows the variation of the rhombohedral lattice parameter and cell angle with time, and Figure 4b shows the equivalent data using the hexagonal cell setting. It is clear from these plots that the structure evolves over the 6.5 h of the experiment. In Figure 3b, the points for experiment 3 (black) show a fractional occupancy of ~0.9 instead of ~0.94, suggesting that the ordering is not fully complete even after 6.5 h. The dependence of the fractional occupancy on time for experiment 3 (see SI, Fig. S2) also shows that the ordering continues to evolve, although at a much slower rate, after ~3.5 h.

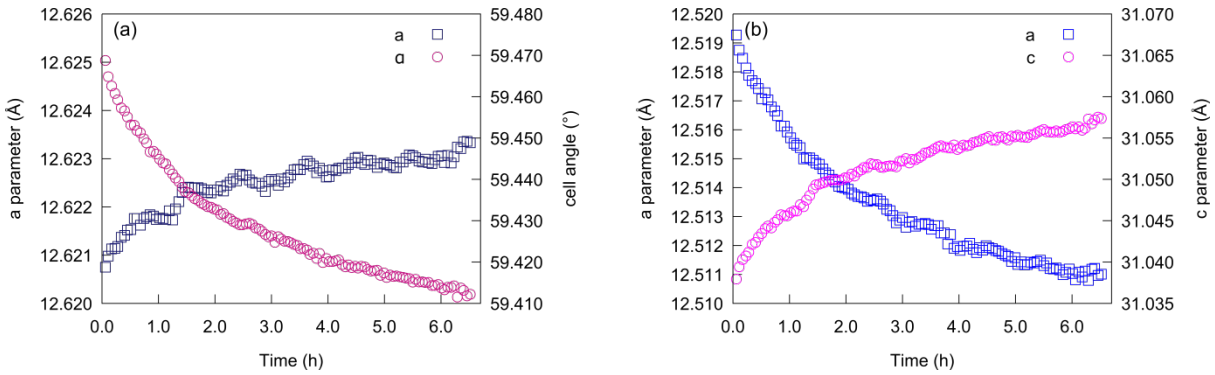

Figure 4. (a) Variation of cell parameters *a* and *α* in rhombohedral setting as a function of time during experiment 3. (b) Data replotted to show the variation of *a* and *c* parameters in an equivalent hexagonal cell setting as a function of time. The total duration of the measurements was ~6.5 h. Typical Rietveld estimated standard deviation values for *a*, *α and c* are 0.0006 Å, 0.003° and 0.001 Å respectively.

3.2 Phase behaviour and entropy changes: experiments 1, 2, 4, 5

The phase evolution observed in each experiment is summarised in Figure 5, where red squares indicate the presence of a cubic phase (*α* at low *T*, *β* at high *T*), green diamonds represent the partially *γ'* (light green) or fully ordered (dark green) *γ* phases, and orange triangles two-phase samples. From these plots, a number of general conclusions about phase stability can be made.

As might be expected from the sluggish nature of the cubic to rhombohedral phase transition, there is some hysteresis in the phase compositions of Figure 5. In particular, the sequence in which isothermal measurements were recorded (compression to 103, 207, 310 MPa followed by decompression to 259, 155, 52 MPa) and the positive slope of the *γ*→*β* boundary means that *γ* phase formed at high *P* may be retained on decompression. It also leads to slight differences in phase composition on cooling relative to heating. Given this dependence on sample history, the compositions reported in Figure 5a-d are reasonable.

It is also clear from Figure 5 that there are some differences between samples prepared by gas-solid and precursor routes. In general, the degree of ordering in *γ'*/*γ* phases is significantly lower for precursor samples and two phase behaviour is more likely. This tendency can also be appreciated from Figure 3b where the cell angle and fractional occupancy values from experiments 4 and 5 (red/purple open points) are clustered more towards the top left of the figure (cubic, disordered) than bottom right (rhombohedral, ordered) than other experiments.

It is clear that all samples retain their as-synthesised phase composition at low temperatures: *α* phases (experiments 1, 4 and 5) remain cubic below ~370 K and the *γ* phase (experiment 2) remains rhombohedral below ~450 K. For the *α* phases a pressure induced transition to the *γ'* or *γ* structures occurs at ~400 K at all pressures. The degree of

ordering is, in general, higher for the gas-solid synthesis (experiment 1) than the precursor syntheses (experiments 4 and 5). At the highest temperature studied, the *γ'*/*γ* phases transform to the cubic *β* phase at all pressures, though there is a clear positive slope to the phase boundary. This is consistent with the smaller volume of the *γ* phase relative to *β* giving a positive sign to $(\partial \Delta G_{dis}/\partial P)_T = \Delta V_{dis}$, making the free energy changes less favourable at high *P*.

Finally, support for the diffraction-derived conclusions of Mo_2O_8 ordering comes from the temperature dependence of the phase boundary between the disordered β phase and ordered *γ*. Whilst this is somewhat influenced by kinetic factors under the experimental conditions used, the "best estimate" boundary is indicated with a dashed line on each of Figure 5a-d. For a 1st order transition, the Clapeyron equation states $(\partial P/\partial T) = \Delta_{trans}\bar{S}/\Delta_{trans}\bar{V}$. Under the assumption that this relationship can be applied to our experiments, from the calculated slope of 3.16 MPa.K^{-1} and volume change of –2.37 cm^{3}mol^{-1} we estimate $\Delta_{trans}\bar{S}$ = –7.5 Jmol^{-1}K^{-1}. If MoO_4 tetrahedra reorient as pairs, the configurational entropy expected for the β to *γ* transition is $-N_A k_B \ln(2)$ = –5.76 Jmol^{-1}K^{-1}. The experimental value is close to this, suggesting that the entropy change is dominated by MoO_4 ordering. The minimum estimate of $\Delta_{trans}\bar{S}$ derived by calorimetry for the equivalent ordering transition in cubic ZrW_2O_8 is –4.1 Jmol^{-1}K^{-1} [40].

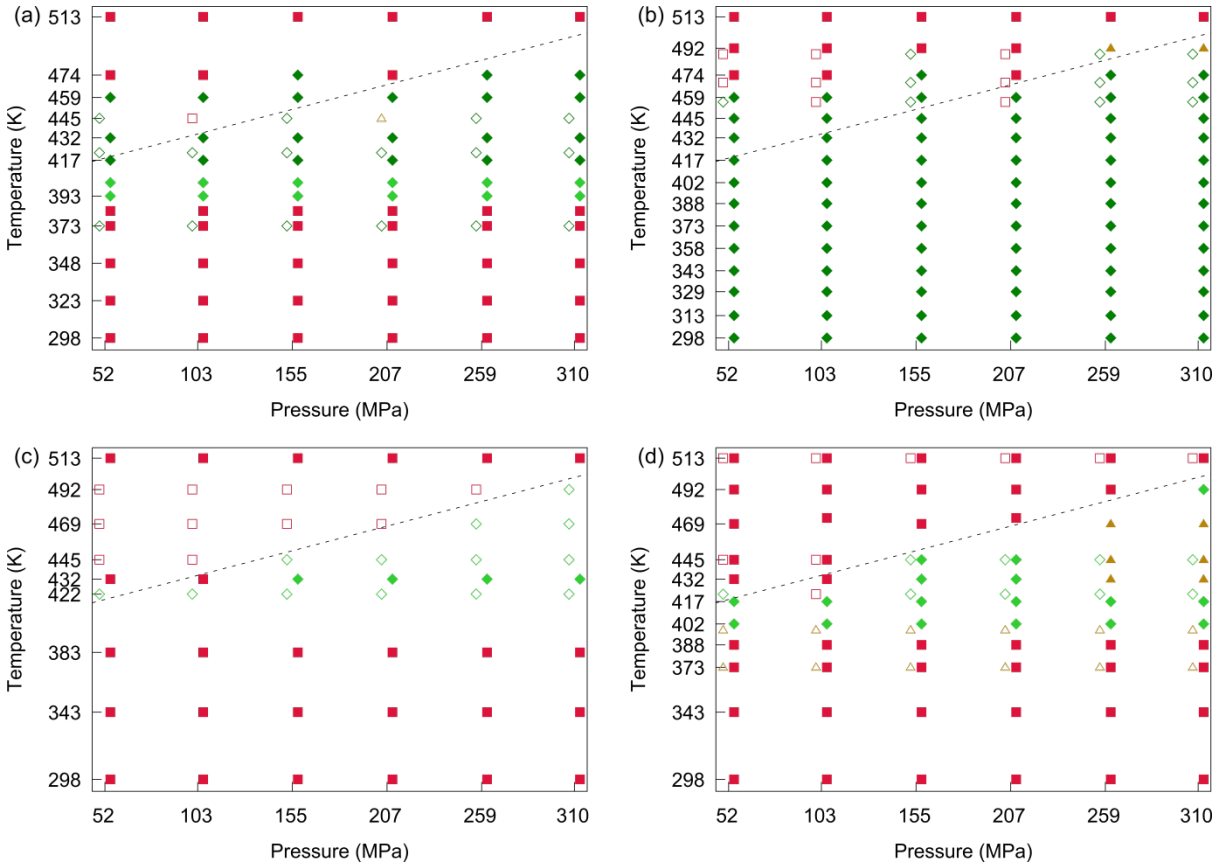

Figure 5. Experimentally observed phase regions for $SnMo_2O_8$ derived from variable *P-T* diffraction experiments. Red symbols represent the cubic phases (*α* at low *T* and *β* at high *T*), light and dark green the rhombohedral *γ*' and *γ* phases respectively, and orange triangles a mixture of cubic and rhombohedral phases. Filled and open symbols represent data collected on heating and cooling, respectively. Data points on warming and cooling have been slightly offset in pressure for clarity (right/left respectively). (a) experiment 1, (b) experiment 2, (c) experiment 4 and (d) experiment 5. Dashed lines denote an approximate phase boundary for *γ*→*β* under compression.

3.3 Thermal expansion behaviour and thermoelastic properties

From the unit cell parameters extracted from the diffraction data of experiments 1 to 5 we can take isothermal cuts to extract the temperature dependence of the bulk modulus or isobaric cuts to derive the pressure dependence of thermal expansion: $B_T = -\left(\frac{\partial P}{\partial lnV}\right)_T$ and $\alpha_P = -\left(\frac{\partial lnV}{\partial T}\right)_P$

In fact, these two quantities are directly related by the expression [2, 41]: $\frac{1}{B^2}\left(\frac{\partial B}{\partial T}\right)_P = \left(\frac{\partial \alpha_V}{\partial P}\right)_T$

and the positive sign of *B* means that a normal material which softens on heating $[(\partial B/\partial T)_P < 0]$ will have a reduced thermal expansion coefficient under applied pressure.

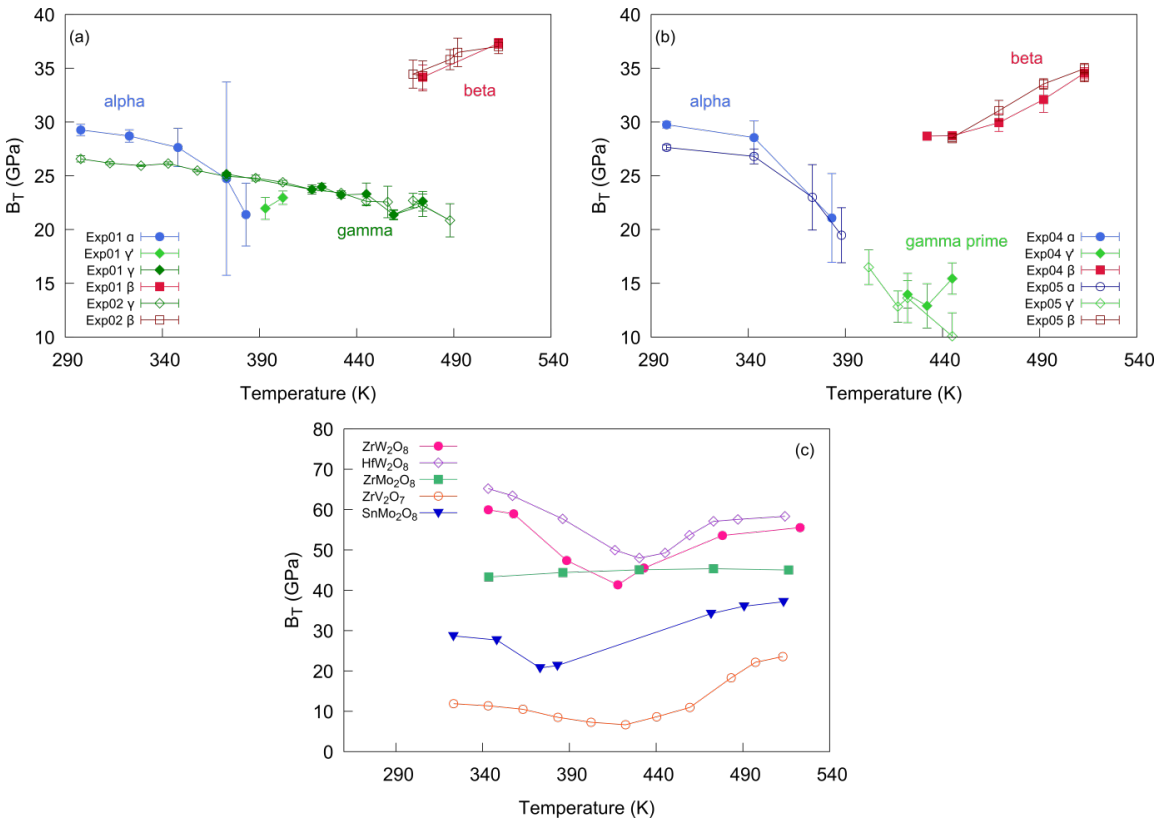

Figure 6. Dependence of isothermal bulk moduli, B_T, of $SnMo_2O_8$ on temperature. (a) Data shown for experiments 1 and 2. (b) Data shown for experiments 4 and 5. The large error bars for some data points are related to the hysteresis between compression and decompression around the temperature region where the phase transition from the *α* to *γ* structure occurs (~370 – 417 K). (c) Values of bulk modulus for cubic AM_2O_8 materials and ZrV_2O_7.

Experimental values of *B* extracted from linear regression of appropriately transformed data for all phases are shown in Figure 6 (see SI for lnV vs *P* plots, Fig. S3). Figure 6a combines data for the samples prepared by the gas-solid route initially in the *α* (experiment 1) or *γ* (experiment 2) phases. Both the *α* and *γ* phases are relatively soft materials (B_{298K} = 29 and 26 GPa respectively) and both soften on heating as normally expected. These values compare to ambient *T* values of 64–75 GPa for ZrW_2O_8 [25, 42-44] and HfW_2O_8 [4, 45] and 43.5 GPa for $ZrMo_2O_8$ [42] (Figure 6c). Where there is experimental overlap good agreement is found between values derived for the *γ* phase in experiment 1 (where it is formed in-situ), and experiment 2 (where it was pre-prepared by annealing at ambient pressure). The larger-volume β phase is significantly stiffer than *α* or *γ* (*B* ≈ 36 GPa) and becomes stiffer still with increasing temperature. For precursor route samples (experiments 4 and 5), the *α* phase displays a similar temperature dependence of *B* within experimental error. The β phase again shows a significant increase in *B* with *T*. Values are slightly lower than those derived in experiments 1 and 2 (e.g. 36 and 33 GPa at 490 K for experiment 2 and experiments 4-5,

respectively). Whilst we cannot be definitive, it seems likely that this is related to the slight differences in the *γ* to β phase boundary and slightly different partial ordering of MoO_4 groups (see below). We have also calculated compressibilites along the *a* and *c* axes in the hexagonal cell setting for the *γ* phase (shown in SI, Fig. S4a-c). Whilst the *c* axis remains unchanged, the compressibility of the *a* axis increases with temperature, and at high *T*, it is almost twice that of the *c* axis.

The bulk modulus of the *γ'* phase in the precursor route samples (Figure 6b) is significantly lower than the *γ* phase (Figure 6a). This is caused by the different kinetics of the phase transition in the materials. For precursor-derived samples a significant component of the compressibility is associated with the negative ΔV_{order} of the cubic to rhombohedral orientational-ordering phase transition that is induced by pressure. Interestingly the bulk modulus of these phases is essentially an extrapolation of the behaviour of the *α* phase suggesting (as in Figure 3) that the *γ'* phase can be viewed as an evolution pathway between the *α* and *γ* phases.

Figure 6c compares experimental data for all cubic AM_2O_8 materials studied to date. We also include the structurally related material ZrV_2O_7 which undergoes a volume-reducing phase transition (ΔV ~0.3 %) where the crystallographically determined V-O-V angle deviates from 180° on either reduction of temperature or increase of pressure [5, 46]. $SnMo_2O_8$ is significantly softer than other AM_2O_8 materials despite the reduction in cell dimension from ZrW_2O_8 (~9.16 Å) to $ZrMo_2O_8$ (~9.13 Å) to $SnMo_2O_8$ (8.96 Å). The phenomenon of temperature induced softening followed by hardening is clearly influenced by the accessibility of volume-reducing phase transitions for all these materials. For the tungstates, this is either cubic $P2_13$ to cubic $Pa\bar{3}$ (for ZrW_2O_8, $\Delta V_{disorder}$~–0.1 %) [10] or cubic to orthorhombic $P2_12_12_1$ (ΔV~–5 %) [26] depending on temperature and pressure. For $SnMo_2O_8$, the transition involves statically disordered to ordered 2×MoO_4 tetrahedral groups and an accompanying volume change caused by coupled rotations of polyhedral groups as the symmetry is lowered. $ZrMo_2O_8$ is unusual amongst these materials in that there is little evidence of MoO_4 orientational order developing on the timescale of experimental studies performed to date [9]. As such its bulk modulus shows only minor pressure dependence [42].

Given the similarity between the thermoelastic properties and the fact that $SnMo_2O_8$ shows positive expansion at all temperatures, the origin of warm hardening is unlikely to be caused by the high anharmonicity mechanism proposed by Dove [2]. The most likely explanation is that it is related to the volume dependence of the order-disorder transition. At the lowest temperatures in the stability field of the disordered β phase, compression will lead to partial ordering of 2×MoO_4 tetrahedral pairs with the accompanying volume reduction giving an

additional component to the compressibility. The tendency to local order will be reduced at higher temperatures due to the increased $T\Delta S$ term, leading to a stiffening of the material.

Values of the thermal expansion coefficient (α_V) as a function of pressure, are plotted for each phase in Figure 7. Given the limited stability field of some phases the uncertainties associated with these values are relatively large. We also observe some "zig-zag" behaviour in values close to phase boundaries where the kinetics of transitions are slow and there is hysteresis caused by the order in which pressure points were recorded (at each *T* in sequence: 103, 207, 310, 259, 155, 52 MPa). The linear coefficients of thermal expansion for the *γ* phase have also been calculated (Fig. S4d in SI) for the *a* and *c* axes in a hexagonal cell setting and, as expected from the results obtained for the compressibilities, the *c* axis remains constant with increasing pressure, and there is a decrease in the α_l with pressure for the *a* axis. Nevertheless we observe that *α* and *γ* phases show the "normal" behaviour of a decrease in thermal expansion under pressure. The β phase (as expected from its warm hardening behaviour) shows an increase in α_V with *P*.

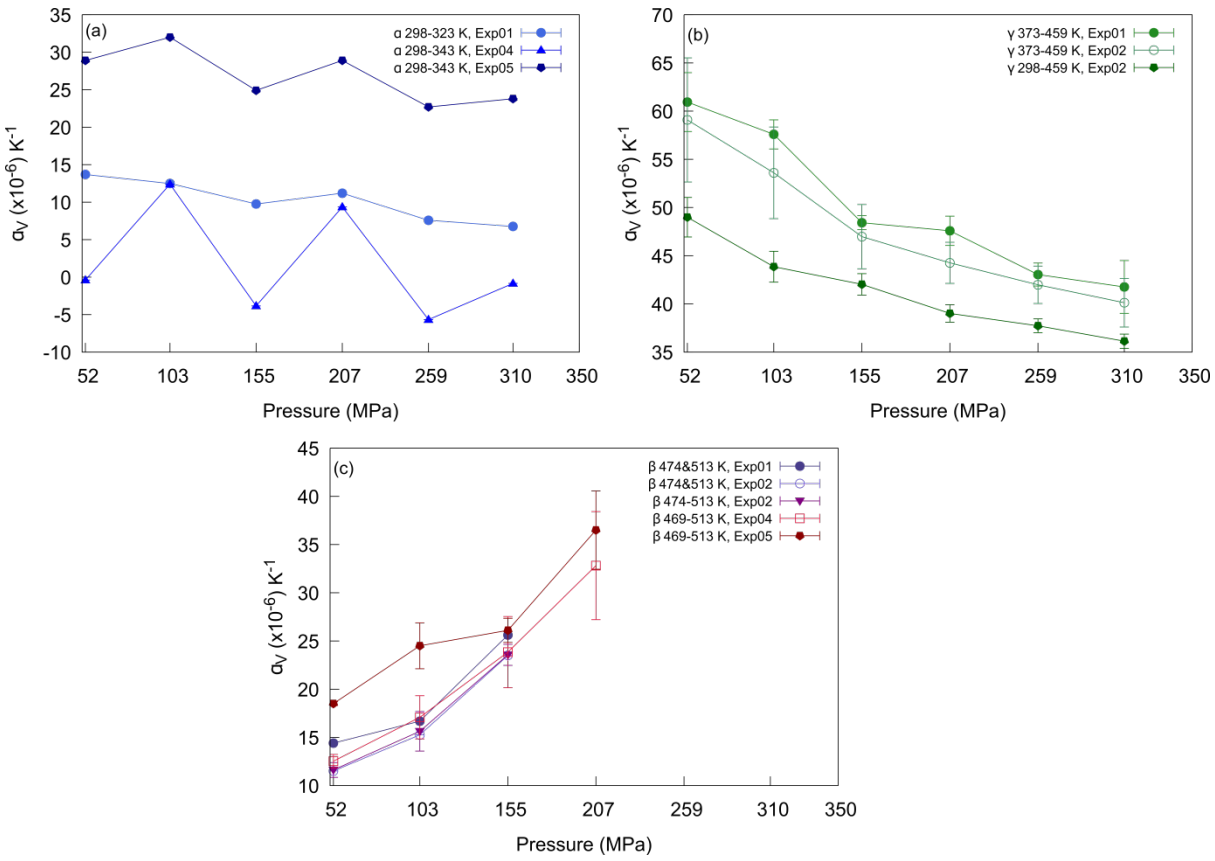

Figure 7. Variation of average volumetric thermal expansion coefficients, α_v, for $SnMo_2O_8$ as a function of pressure. (a) Data for *α*-$SnMo_2O_8$, (b), data for *γ*-$SnMo_2O_8$, and (c), data for *β*-$SnMo_2O_8$. Error bars are not included in (a) where only two data points are available for extracting α_v.

4. Conclusions

In conclusion, in-situ x-ray diffraction studies have revealed the behaviour of the kinetically stable phases of $SnMo_2O_8$ at temperatures and pressures relevant for applications; T = 298 K to 513 K and P = ambient to 310 MPa. The α, γ', γ and β phases are found in this regime with β at high T and either α, γ', or the most stable γ at the lower temperatures or higher pressures depending on the thermal and pressure history of the sample. Diffraction data suggest an essentially continuous evolution from disordered Mo_2O_8 groups in α-$SnMo_2O_8$ to ordered groups in γ-$SnMo_2O_8$ is possible. At temperatures and pressures close to the $\alpha \rightarrow \gamma$ and $\gamma \rightarrow \beta$ boundaries, phase transitions can be relatively sluggish occurring over timescales of minutes to days. In general, precursor-route samples have slower transformation kinetics than gas-solid samples, suggesting that there are differences in their defect chemistry or local structure. All $SnMo_2O_8$ phases are relatively soft with bulk moduli of β (~36 GPa) > α (~29 GPa) > γ (~26 GPa) > γ' (~15 GPa). Overall, bulk moduli drop as samples are warmed towards the temperature at which the kinetics of Mo_2O_8 ordering to give the γ polymorph become favourable. This implies that the softening is linked to local fluctuations towards the lower-volume ordered Mo_2O_8 structure and later hardening due to these fluctuations becoming less prevalent. The gamma phase shows anisotropy in compressibility: when using a hexagonal description, the *a*-axis is ~30 % more compressible than the *c*-axis. The α and γ phases show a reduction in thermal expansion coefficient with pressure as found for most materials. The β phase shows a less common increase in thermal expansion with pressure, consistent with it becoming stiffer on heating.

5. Acknowledgments

This research used resources of the Advanced Photon Source, a U.S. Department of Energy (DOE) Office of Science User Facility operated for the DOE Office of Science by Argonne National Laboratory under Contract No. DE-AC02-06CH11357. We are grateful for the assistance of Brett R. Hester, Benjamin S. Kaplan and beamline staff Karena W. Chapman and Kevin A. Beyer. LRA and JSOE gratefully acknowledge the Brazilian National Council for Scientific and Technological Development (CNPq) and the Ciência Sem Fronteiras (CsF) program for financial support (PhD studentship of LRA). Funding was also provided by the Georgia Institute of Technology.

6. References

[1] S.E. Tallentire, F. Child, I. Fall, L. Vella-Zarb, I.R. Evans, M.G. Tucker, D.A. Keen, C. Wilson, J.S.O. Evans, Systematic and Controllable Negative, Zero, and Positive Thermal Expansion in Cubic $Zr_{1-x}Sn_xMo_2O_8$, Journal of the American Chemical Society 135(34) (2013) 12849-12856.

[2] M.T. Dove, H. Fang, Negative thermal expansion and associated anomalous physical properties: review of the lattice dynamics theoretical foundation, Reports on progress in physics. Physical Society 79(6) (2016) 066503.
[3] C.R. Morelock, L.C. Gallington, A.P. Wilkinson, Solid solubility, phase transitions, thermal expansion, and compressibility in $Sc_{1-x}Al_xF_3$, Journal of Solid State Chemistry 222 (2015) 96-102.
[4] L.C. Gallington, K.W. Chapman, C.R. Morelock, P.J. Chupas, A.P. Wilkinson, Dramatic softening of the negative thermal expansion material HfW_2O_8 upon heating through its WO_4 orientational order-disorder phase transition, Journal of Applied Physics 115(5) (2014) 053512.
[5] L.C. Gallington, B.R. Hester, B.S. Kaplan, A.P. Wilkinson, Pressure-dependence of the phase transitions and thermal expansion in zirconium and hafnium pyrovanadate, Journal of Solid State Chemistry 249 (2017) 46-50.
[6] T.A. Mary, J.S.O. Evans, T. Vogt, A.W. Sleight, Negative Thermal Expansion from 0.3 to 1050 Kelvin in ZrW_2O_8, Science 272 (1996) 90-92.
[7] J.S.O. Evans, T.A. Mary, T. Vogt, M.A. Subramanian, A.W. Sleight, Negative Thermal Expansion in ZrW_2O_8 and HfW_2O_8, Chemistry of Materials 8(12) (1996) 2809-2823.
[8] C. Lind, A.P. Wilkinson, Z. Hu, S. Short, J.D. Jorgensen, Synthesis and Properties of the Negative Thermal Expansion Material Cubic $ZrMo_2O_8$, Chemistry of Materials 10(9) (1998) 2335-2337.
[9] S. Allen, J.S.O. Evans, Negative thermal expansion and oxygen disorder in cubic $ZrMo_2O_8$, Physical Review B 68(13) (2003) 134101.
[10] J.S.O. Evans, W.I.F. David, A.W. Sleight, Structural investigation of the negative-thermal-expansion material ZrW_2O_8, Acta Crystallographica Section B 55(3) (1999) 333-340.
[11] G.D. Barrera, J.A.O. Bruno, T.H.K. Barron, N.L. Allan, Negative thermal expansion, Journal of Physics: Condensed Matter 17(4) (2005) R217-R252.
[12] K.T. Hammonds, M.T. Dove, A.P. Giddy, V. Heine, B. Winkler, Rigid-unit phonon modes and structural phase transitions in framework silicates, American Mineralogist 81 (1996) 1057-1079.
[13] A.K.A. Pryde, K.T. Hammonds, M.T. Dove, V. Heine, J.D. Gale, M.C. Warren, Origin of the negative thermal expansion in ZrW_2O_8 and ZrV_2O_7, Journal of Physics: Condensed Matter 8(50) (1996) 10973.
[14] M.G. Tucker, D.A. Keen, J.S. Evans, M.T. Dove, Local structure in ZrW_2O_8 from neutron total scattering, Journal of Physics: Condensed Matter 19(33) (2007) 335215.
[15] L.H.N. Rimmer, M.T. Dove, K. Refson, The negative thermal expansion mechanism of zirconium tungstate, ZrW_2O_8, arXiv:1510.00361, 2015.
[16] L.H.N. Rimmer, M.T. Dove, Simulation study of negative thermal expansion in yttrium tungstate $Y_2W_3O_{12}$, Journal of Physics: Condensed Matter 27(18) (2015) 185401.
[17] C. Pantea, A. Migliori, P.B. Littlewood, Y. Zhao, H. Ledbetter, J.C. Lashley, T. Kimura, J. Van Duijn, G.R. Kowach, Pressure-induced elastic softening of monocrystalline zirconium tungstate at 300K, Physical Review B 73(21) (2006) 214118.
[18] K.W. Chapman, P.J. Chupas, Pressure Enhancement of Negative Thermal Expansion Behavior and Induced Framework Softening in Zinc Cyanide, Journal of the American Chemical Society 129(33) (2007) 10090-10091.
[19] R. Miletich, G.D. Gatta, T. Willi, P.W. Mirwald, P. Lotti, M. Merlini, N. Rotiroti, T. Loerting, Cordierite under hydrostatic compression: Anomalous elastic behavior as a precursor for a pressure-induced phase transition, American Mineralogist 99(2-3) (2014) 479-493.
[20] O.B. Tsiok, V.V. Brazhkin, A.G. Lyapin, L.G. Khvostantsev, Logarithmic Kinetics of the Amorphous-Amorphous Transformations in SiO_2 and GeO_2 Glasses under High Pressure, Physical review letters 80(5) (1998) 999-1002.
[21] M.W. Andrew, A.S. Lucy, T. Kostya, P.B. Richard, O.H.W. Toby, T.D. Martin, P.T. Richard, T.T. Ilian, A.W. Stephen, The origin of the compressibility anomaly in amorphous silica: a molecular dynamics study, Journal of Physics: Condensed Matter 19(27) (2007) 275210.

[22] R. Mittal, S.L. Chaplot, H. Schober, T.A. Mary, Origin of negative thermal expansion in cubic ZrW_2O_8 revealed by high pressure inelastic neutron scattering, Physical review letters 86(20) (2001) 4692-5.
[23] R. Mittal, S.L. Chaplot, H. Schober, A.I. Kolesnikov, C.K. Loong, C. Lind, A.P. Wilkinson, Negative thermal expansion in cubic $ZrMo_2O_8$: Inelastic neutron scattering and lattice dynamical studies, Physical Review B 70(21) (2004) 214303.
[24] G. Ernst, C. Broholm, G.R. Kowach, A.P. Ramirez, Phonon density of states and negative thermal expansion in ZrW_2O_8, Nature 396(6707) (1998) 147-149.
[25] F.R. Drymiotis, H. Ledbetter, J.B. Betts, T. Kimura, J.C. Lashley, A. Migliori, A.P. Ramirez, G.R. Kowach, J. Van Duijn, Monocrystal elastic constants of the negative-thermal-expansion compound zirconium tungstate (ZrW_2O_8), Physical review letters 93(2) (2004) 025502.
[26] J.D. Jorgensen, Z. Hu, S. Teslic, D.N. Argyriou, S. Short, Pressure-induced cubic-to-orthorhombic phase transition in ZrW_2O_8, Physical Review B 59(1) (1999) 215-225.
[27] C.A. Perottoni, J.A.H. Jornada, Pressure-Induced Amorphization and Negative Thermal Expansion in ZrW_2O_8, Science 280 (1998) 886-889.
[28] A. Grzechnik, W.A. Crichton, K. Syassen, P. Adler, M. Mezouar, A New Polymorph of ZrW_2O_8 Synthesized at High Pressures and High Temperatures, Chemistry of Materials 13(11) (2001) 4255-4259.
[29] C. Lind, D.G. Vanderveer, A.P. Wilkinson, J. Chen, M.T. Vaughan, D.J. Weidner, New-high pressure form of the negative thermal expasion materials Zirconium Molybdate and Hafnium Molybdate, Chemistry of Materials 13 (2001) 487-490.
[30] A. Grzechnik, W.A. Crichton, Structural transformations in cubic $ZrMo_2O_8$ at high pressures and high temperatures, Solid State Sciences 4(9) (2002) 1137-1141.
[31] S. Carlson, A.M.K. Andersen, High-pressure transitions of trigonal α-$ZrMo_2O_8$, Physical Review B 61(17) (2000) 11209-11212.
[32] A.M. Krogh Andersen, S. Carlson, High-pressure structures of α- and δ-$ZrMo_2O_8$, Acta Crystallographica Section B 57(1) (2001) 20-26.
[33] D.V.S. Muthu, B. Chen, J.M. Wrobel, A.M. Krogh Andersen, S. Carlson, M.B. Kruger, Pressure-induced phase transitions in α−$ZrMo_2O_8$, Physical Review B 65(6) (2002) 064101.
[34] R.M. Hazen, A. Navrotsky, Effects of pressure on order-disorder reactions, American Mineralogist 81(9-10) (1996) 1021-1035.
[35] J. Buiten, Preparation of crystalline tin(IV) molybdate having an unexpectedly low density, Polyhedron 7 (1988) 585-586.
[36] M.R. Hampson, J.S.O. Evans, P. Hodgkinson, Characterization of Oxygen Dynamics in ZrW_2O_8, Journal of American Chemical Society 127(43) (2005) 15175-15181.
[37] A.P. Wilkinson, C.R. Morelock, B.K. Greve, A.C. Jupe, K.W. Chapman, P.J. Chupas, C. Kurtz, Reducing the background from pressure vessels using a BRIM, Journal of Applied Crystallography 44(5) (2011) 1047-1053.
[38] A.A. Coelho, TOPAS Academic: General Profile and Structure Analysis Software for Powder Diffraction Data, Bruker AXS, Karlsruhe, Germany, 2012.
[39] A.A. Coelho, J. Evans, I. Evans, A. Kern, S. Parsons, The TOPAS symbolic computation system, Powder Diffraction 26(S1) (2012) S22-S25.
[40] Y. Yamamura, T. Tsuji, K. Saito, M. Sorai, Heat capacity and order–disorder phase transition in negative thermal expansion compound ZrW_2O_8, The Journal of Chemical Thermodynamics 36(6) (2004) 525-531.
[41] O.L. Anderson, Equations of State of Solids for Geophysics and Ceramic Science, Oxford University Press, Oxford, 1995.
[42] L.C. Gallington, K.W. Chapman, C.R. Morelock, P.J. Chupas, A.P. Wilkinson, Orientational order-dependent thermal expansion and compressibility of ZrW_2O_8 and $ZrMo_2O_8$, Physical chemistry chemical physics : PCCP 15(45) (2013) 19665-72.
[43] J.S.O. Evans, Z. Hu, J.D. Jorgensen, D.N. Argyriou, S. Short, A.W. Sleight, Compressibility, phase transitions, and oxygen migration in zirconium tungstate, ZrW_2O_8, Science 275(5296) (1997) 61-65.

[44] J.S.O. Evans, J.D. Jorgensen, S. Short, W.I.F. David, R.M. Ibberson, A.W. Sleight, Thermal expansion in the orthorhombic gamma phase of ZrW_2O_8, Physical Review B 60(21) (1999) 14643-14648.
[45] J.D. Jorgensen, Z. Hu, S. Short, A.W. Sleight, J.S.O. Evans, Pressure-induced cubic-to-orthorhombic phase transformation in the negative thermal expansion material HfW_2O_8, Journal of Applied Physics 89(6) (2001) 3184-3188.
[46] R.L. Withers, J.S.O. Evans, J. Hanson, A.W. Sleight, An in SituTemperature-Dependent Electron and X-ray Diffraction Study of Structural Phase Transitions in ZrV_2O_7, Journal of Solid State Chemistry 137(1) (1998) 161-167.